



Key factors in Sr-doped LaBO₃ (B=Co or Mn) perovskites for NO oxidation in efficient diesel exhaust purification

Jon A. Onrubia-Calvo, B. Pereda-Ayo, U. De-La-Torre, Juan R. González-Velasco*

Departamento de Ingeniería Química, Facultad de Ciencia y Tecnología, Universidad del País Vasco, UPV/EHU, Campus de Leioa, P.O. Box 644, ES-48080 Bilbao, Bizkaia, Spain

ARTICLE INFO

Article history:

Received 14 February 2017

Received in revised form 19 April 2017

Accepted 24 April 2017

Available online 1 May 2017

Keywords:

Perovskite

LaCoO₃

LaMnO₃

Sr-doping

Surface oxygen vacancies

NO oxidation

Pt-free catalyst

ABSTRACT

Perovskites have attracted attention in recent years as an economic alternative to noble metals in oxidation processes. Synthesis conditions of LaCoO₃ and LaMnO₃ perovskites have been studied varying citrate to nitrate molar ratio in the starting solution, pH and calcination protocol, with the aim of obtaining high purity perovskites, absence of impurities, and with enhanced textural properties. Once synthesis conditions were established, strontium was incorporated in the perovskite lattice as a textural and structural promoter, by substituting lanthanum with different doping levels, i.e. La_{0.9}Sr_{0.1}BO₃, La_{0.8}Sr_{0.2}BO₃, La_{0.7}Sr_{0.3}BO₃, La_{0.6}Sr_{0.4}BO₃ and La_{0.5}Sr_{0.5}BO₃ with B=Co or Mn. The prepared solids were characterized in terms of crystalline phase identification (XRD), specific surface area (N₂ adsorption-desorption at -196 °C), reducibility and oxidation state of transition metal ions (H₂-TPR), quantification of adsorbed oxygen species (O₂-TPD) and surface elemental composition (XPS). Charge imbalance associated to strontium (Sr²⁺) incorporation in the perovskite lattice in substitution of lanthanum (La³⁺) was preferentially balanced by Mn⁴⁺ promotion in La_{1-x}Sr_xMnO₃ perovskites, whereas formation of oxygen vacancies seems to be the mechanism for charge compensation in La_{1-x}Sr_xCoO₃ perovskites, where Co ions remained as Co³⁺ ions. Strontium doped perovskites further improved NO conversion compared to the non-substituted formulations. The best NO oxidation performance was obtained with La_{0.7}Sr_{0.3}CoO₃ and La_{0.9}Sr_{0.1}MnO₃ samples, achieving maximum NO conversion of 83 and 65% at 300 and 325 °C, respectively. Higher oxidation capacity of La_{0.7}Sr_{0.3}CoO₃ sample was associated to the higher oxygen mobility and exchange capacity between oxygen in the lattice and gas phase oxygen. It is worth noting that prepared perovskites presented far higher NO oxidation capacity than platinum-based NSR model catalysts, confirming perovskites as an economic alternative to catalyze NO oxidation reactions in automotive catalysis.

© 2017 Elsevier B.V. All rights reserved.

1. Introduction

Diesel engines present higher fuel efficiency than stoichiometric gasoline engines and thereby emit less CO₂ to the atmosphere. In contrast, the clean-up of diesel exhaust gases is even more challenging than gasoline engines exhaust gases, due to the nature of the emission, including soot, and also due to the net oxidizing environment that limits NO_x reduction [1]. In order to meet stringent emission standards, diesel engines implemented catalytic processes such as Diesel Oxidation Catalyst (DOC) [2] or Diesel Particulate Filter (DPF) [3]. In the DOC, unburned hydrocarbons as well as carbon monoxide are completely oxidized to CO₂ and H₂O while NO is converted into NO₂. Afterwards, soot is trapped

in DPF and continuously regenerated by oxidation with NO₂ produced in the DOC. However, this strategy fails in meeting EURO VI standards regarding NO_x emissions, and consequently additional catalytic strategies are mandatory to be implemented, such as NO_x Storage and Reduction (NSR) [4] or Selective Catalytic Reduction (SCR) [5]. In the NSR technology, NO-to-NO₂ oxidation is considered a primary step to promote NO_x storage via nitrites or nitrates [6,7] formed over an alkali or alkali-earth material, because NO₂ adsorption occurs much faster than NO [4]. In the SCR technology NO-to-NO₂ oxidation is also of critical importance [8] being well known that the fast SCR reaction activates when NO/NO₂ = 1/1 (molar ratio), achieving high NO_x conversion even at lower temperature. Thus, the significance of NO-to-NO₂ oxidation reaction in automotive exhaust purification is relevant and merits further research on novel catalyst formulations.

Noble metal based catalysts have been commonly employed in order to promote NO oxidation in automotive catalysis. How-

* Corresponding author.

E-mail address: juanra.gonzalezvelasco@ehu.es (J.R. González-Velasco).

ever, the use of noble metal (especially Pt) results in high cost and poor thermal stability under highly oxidative conditions [9]. In that sense, perovskites have attracted attention in recent years as potential, low-cost alternative to noble metal in oxidation processes [10]. In the perovskite lattice (with the general formula ABO_3), the B cation coordinates with oxygen in octahedral structure, and A cation locates in the center of the dodecahedral structure. Perovskites activity for oxidation reactions seems to be related with some specific structural properties, such as change of oxidation state of B cation, active oxygen mobility and ion vacancy defect [11]. During oxidation reactions, lattice oxygen is thought to be catalytically active and its consumption and regeneration is relative to cycling the oxidation state of neighboring transition metal ions ($\text{B}^{3+} \leftrightarrow \text{B}^{4+}$) and/or ($\text{B}^{2+} \leftrightarrow \text{B}^{3+}$) [12]. In that sense, it has been reported that the catalytic activity of perovskites is far influenced by the type of B cation and its oxidation state cycling feasibility [13].

LaMnO_3 and LaCoO_3 perovskites have been proposed as active perovskites for NO oxidation reactions [11,14]. In particular, LaMnO_3 perovskite is somewhat unusual in that $\text{Mn}^{3+}/\text{Mn}^{4+}$ mixed oxidation state is usually observed even for nominal stoichiometry $\text{LaMnO}_{3+\delta}$ (with Mn^{4+} content of 2δ per formula unit), opposite to most other perovskites. However, it has been proposed that electroneutrality of the lattice is accomplished by generating cation vacancies, instead of oxygen over-stoichiometry, as perovskite lattice cannot accommodate interstitial oxygen ions [15,16]. On the other hand, stoichiometric LaCoO_3 perovskite usually presents some oxygen deficiency in the lattice, represented by $\text{LaCoO}_{3-\delta}$, and the charge balance is accomplished by the presence of some cobalt as Co^{2+} . This $\text{Mn}^{3+}/\text{Mn}^{4+}$ and $\text{Co}^{2+}/\text{Co}^{3+}$ reversible oxidation state is thought to be a key factor for oxidation reactions [17–20].

The oxidation state of B cation can be modulated by varying preparation steps during the perovskite synthesis, such as calcination temperature [21], non-stoichiometry of cations A or B [12,14] or substituting La^{3+} by lower oxidation state cations, such as Ca^{2+} , Ba^{2+} or Sr^{2+} , or even higher oxidation state cation such as Ce^{4+} . Strontium-doped LaMnO_3 and LaCoO_3 perovskites have been used for a wide range of applications [10,22–24]. The introduction of lower oxidation state Sr^{2+} in substitution of La^{3+} in LaMnO_3 and LaCoO_3 lattice generates a net charge imbalance that may be compensated by alteration of the oxidation state of a fraction of transition metal, e.g. Mn^{4+} or Co^{4+} . Alternatively, the oxidation state of transition metal could be maintained unaltered (Mn^{3+} or Co^{3+}), but instead oxygen vacancies could be generated in the lattice to attain the charge balance. Even a mixed situation showing altered oxidation state of transition metal along with oxygen vacancies in the lattice could be expected.

Oxide-based catalysts have typically shown much lower activity than Pt-based catalysts under the kinetics-controlled temperature regime. However, Kim et al. [25] prepared $\text{La}_{0.9}\text{Sr}_{0.1}\text{CoO}_3$ and $\text{La}_{0.9}\text{Sr}_{0.1}\text{MnO}_3$ perovskites and reported NO oxidation activity similar to or higher than those of Pt-based catalysts under realistic automotive conditions. Li et al. [26] prepared a series of $\text{La}_{1-x}\text{Sr}_x\text{CoO}_3$ ($x=0.1, 0.2, 0.3, 0.4$ and 0.5), and they found, after the NO_x storage tests, the $\text{La}_{0.7}\text{Sr}_{0.3}\text{CoO}_3$ perovskite had the best NO-to- NO_2 performance and the largest NO_x storage capacity (NSC) at 300°C . These authors also suggested possible NO_x storage routes on $\text{La}_{1-x}\text{Sr}_x\text{CoO}_3$. To our knowledge, a similar study of strontium-doped Mn-based perovskites has not been reported and results compared with those of Co-based perovskites.

More recently, Dong et al. [22] prepared a series of $\text{La}_{0.7}\text{Sr}_{0.3}\text{MnO}_3$ perovskite-type catalysts by the sol-gel method using citric acid as the complexant. They concluded that variation of synthesis conditions, namely the calefactive velocity, the calcination temperature and the pH of the precursor solutions, greatly affect the morphology of the perovskite catalyst and, consequently,

the NO-to- NO_2 activity and NO_x storage capacity of $\text{La}_{0.7}\text{Sr}_{0.3}\text{MnO}_3$ perovskite-type catalysts.

In this work, we look deeply into the identification of the main changes in physico-chemical properties induced by the modification of different parameters (i.e. synthesis conditions or lanthanum partial substitution by strontium). Consequently, relevant information on the key factors for the NO-to- NO_2 oxidation is extracted, along with the main differences derived from the chemical nature of B cation (Co or Mn) in the perovskite-based catalyst. This information would allow designing noble-metal-free catalysts competitive to substitute conventional Pt-containing NSR catalysts. We prepare, characterize and test NO oxidation activity of stoichiometric LaMnO_3 and LaCoO_3 as well as strontium doped $\text{La}_{1-x}\text{Sr}_x\text{MnO}_3$ and $\text{La}_{1-x}\text{Sr}_x\text{CoO}_3$ perovskites ($x=0.1, 0.2, 0.3, 0.4$ and 0.5). Firstly, the study focuses on the optimizing of the synthesis conditions during the sol-gel process to improve the oxidation capacity, including citrate to nitrate ratio, pH of the gel and calcination protocol to get pure perovskites with no phase segregation and enhanced textural properties; then special attention is focused on the correlation of NO-to- NO_2 activity with the physico-chemical properties of the prepared strontium-doped perovskite-based catalysts.

2. Experimental

2.1. Perovskite catalyst preparation

All perovskites were prepared the by citric acid sol-gel method [27]. Appropriate amounts of $\text{La}(\text{NO}_3)_3 \cdot 6\text{H}_2\text{O}$ (Fluka), $\text{Co}(\text{NO}_3)_2 \cdot 6\text{H}_2\text{O}$ (Sigma Aldrich), $\text{Mn}(\text{NO}_3)_2 \cdot 4\text{H}_2\text{O}$ (Merck) were dissolved in distilled water under vigorous stirring. Then citric acid ($\text{C}_6\text{H}_8\text{O}_7 \cdot \text{H}_2\text{O}$, CA) was added as a complexing agent and organic loading for the combustion process with a citrate to nitrate (CA/N) molar ratios of 0.7, 1.1 or 1.5. The pH value was adjusted to 3, 4.5, 6, 7, 8 or 9 by ammonia (25% as NH_3 , Panreac). After solvent evaporation at 80°C , the gel was further dried at 120°C overnight and then calcined in 5% O_2/He (60 mL min^{-1}) or static air at desired temperature (600°C , 700°C , 800°C or 900°C) for 4 h. Table 1 resumes the nomenclature and synthesis conditions of all catalyst. The general nomenclature set for each sample was as follows: LaCoO_3 (LCO) or LaMnO_3 (LMO) with the specific synthesis conditions in brackets (citrate to nitrate molar ratio/pH/calcination temperature), as for example LCO (1.1/7/700). In order to determine if the synthesis method was repetitive this sample was prepared twice (with + in Table 1).

In order to synthesize strontium doped $\text{La}_{1-x}\text{Sr}_x\text{CoO}_3$ and $\text{La}_{1-x}\text{Sr}_x\text{MnO}_3$ perovskites, adequate amount of $\text{Sr}(\text{NO}_3)_2$ (Sigma Aldrich) was added to the initial solution following the same procedure as stated before. The following samples with increasing La substitution degree by Sr were synthetized: $\text{La}_{0.9}\text{Sr}_{0.1}\text{BO}_3$, $\text{La}_{0.8}\text{Sr}_{0.2}\text{BO}_3$, $\text{La}_{0.7}\text{Sr}_{0.3}\text{BO}_3$, $\text{La}_{0.6}\text{Sr}_{0.4}\text{BO}_3$, $\text{La}_{0.5}\text{Sr}_{0.5}\text{BO}_3$, with B = Mn or Co.

A Pt-based catalyst (1.5% Pt–15% $\text{BaO}/\text{Al}_2\text{O}_3$) was prepared as a reference by consecutive wetness impregnation. Firstly, a specific load of platinum (1.5%) was incorporated to the alumina support by dissolving the adequate amount of trettaammineplatinum (II) nitrate [$\text{Pt}(\text{NH}_3)_4(\text{NO}_3)_2$] on distillate water. Then, the same process was repeated for barium incorporation (15%) using the adequate amount of barium acetate [$\text{Ba}(\text{CH}_3\text{COO})_2$] as precursor. After each impregnation, the catalyst was calcined at 500°C for 4 h.

2.2. Catalyst characterization

X-ray diffraction (XRD) patterns were obtained on a Philips PW1710 diffractometer. The samples were finely ground and were

Table 1

Nomenclature, synthesis conditions and textural properties of the prepared LaCoO_3 and LaMnO_3 perovskites.

Perovskite	Nomenclature	CA/N	pH	T. Calc., °C	SSA, $\text{m}^2 \text{g}^{-1}$	d_c , nm
LaCoO_3	LCO (0.7/7/700)	0.7	7	700	5.1	51
	LCO (1.1/7/700)	1.1	7	700	10.6	40
	LCO (1.5/7/700)	1.5	7	700	10.1	67
	LCO (1.1/3/700)	1.1	3	700	11.3	57
	LCO (1.1/4.5/700)	1.1	4.5	700	9.7	45
	LCO (1.1/6/700)	1.1	6	700	9.7	41
	LCO (1.1/8/700)	1.1	8	700	12.6	38
	LCO (1.1/9/700)	1.1	9	700	13.2 (15.2 ^a)	46 (34 ^a)
	LCO (1.1/7/600)	1.1	7	600	14.6	24
	LCO (1.1/7/700) ^a	1.1	7	700	11.0 (11.6 ^a)	41 (39 ^a)
LaMnO_3	LMO (1.1/4.5/700)	1.1	4.5	700	21.6	42
	LMO (1.1/6/600)	1.1	6	600	31.3	31
	LMO (1.1/6/700)	1.1	6	700	26.0	34
	LMO (1.1/7/700)	1.1	7	700	23.0	45
	LMO (1.1/8/700)	1.1	8	700	13.9	51

^a Calcination in 5% O_2/He flow.

subjected to Cu K_{α} radiation in a continuous scan mode from 5° to $70^\circ 2\theta$ with 0.02° per second sampling interval. PANalytical X'pert HighScore specific software was used for data treatment.

Textural properties of the samples were determined by N_2 adsorption-desorption at -196°C using Micromeritics TriStar equipment.

The thermogravimetric (TG) analysis was conducted with Setaram Setsys Evolution TG instrument coupled to the mass spectrometer Pfeiffer Vacuum DUO 2.5, using 10 mg of sample. The experiment was conducted in 5% O_2/He mixture or air (100 mL min^{-1}) from room temperature to 950°C at a heating rate of 2°C min^{-1} .

The reducibility of the samples was investigated by temperature programmed reduction (H_2 -TPR) using Micromeritics AutoChem II equipment. The quartz tube reactor was loaded with 0.1 g of sample and pretreated with 30 mL min^{-1} of 5% O_2/He mixture at 600°C for 30 min, and then cooled down to 50°C . Afterwards, samples were heated from room temperature to 900°C with $10^\circ\text{C min}^{-1}$ heating rate in a 5% H_2/Ar gas mixture with 30 mL min^{-1} flowrate. Water generated during sample reduction was removed using a cold trap before gas analysis by TCD.

The strength and concentration of different oxygen species was investigated by Oxygen temperature programmed desorption (O_2 -TPD) using Micromeritics AutoChem II equipment. The sample (0.1 g) was introduced in a quartz tube reactor and pretreated with 50 mL min^{-1} of 5% O_2/He mixture at 600°C for 5 min and then cooled down to 40°C . Afterwards, samples were heated from room temperature to 900°C with a heating rate of $10^\circ\text{C min}^{-1}$ in a 50 mL min^{-1} of Helium gas flow.

X-ray photoelectronic spectroscopy (XPS) characterization was carried out in a SPECS electron spectrometer with a Phoibos 150 1D-DLD energy analyzer using Al-K α (1486.7 eV) radiation source. To obtain the XPS spectra, the pressure of the analysis chamber was maintained at 5×10^{-10} mbar. The binding energy (BE) scale was adjusted by setting the C 1s transition at 284.6 eV.

2.3. NO-to-NO₂ oxidation experiments

Oxidation tests were carried out in a vertical stainless steel reactor filled with 0.5 grams of 0.3–0.5 mm pelletized catalyst, and placed inside a 3-zone tube furnace. The feed composition was 650 ppm of NO, 6% O₂ and Ar as balance gas. Gases were feed via mass flow controllers and the total flow rate was set at

634 mL min^{-1} , which corresponded to a space velocity (GHSV) of $123,500 \text{ h}^{-1}$. Temperature was measured by a thermocouple inside the catalyst bed.

The outlet gas composition was continuously measured using a MKS MultiGas 2030 FT-IR analyzer for quantitative analysis of NO and NO₂ (no additional nitrogen compounds are detected). The conversion of NO-to-NO₂ was calculated after steady state at even temperature was reached, which usually needed around 20 min after temperature stabilization, according to Eq. (1):

$$X_{\text{NO-to-NO}_2}(\%) = \frac{F_{\text{NO}}^{\text{in}} - F_{\text{NO}}^{\text{out}}}{F_{\text{NO}}^{\text{in}}} \times 100 \quad (1)$$

3. Results and discussion

3.1. Preparation, characterization and NO oxidation activity of LaCoO_3 and LaMnO_3 perovskites

There are several parameters affecting perovskites physico-chemical properties during the synthesis, such as citrate to nitrate molar ratio in the starting solution, pH value of the gel and calcination protocol [22,28–30]. The influence of the preparation procedure on the physico-chemical properties on LaCoO_3 and LaMnO_3 perovskites was analyzed by thermogravimetric analysis (Fig. S1), X-ray diffraction (Figs. S2 and S3), temperature programmed hydrogen reduction (Fig. S4) and textural properties. The main characterization results of the prepared catalysts are summarized in Table 1.

The influence of citrate to nitrate ratio (CA/N) was studied by preparing LaCoO_3 perovskite with a citrate to nitrate molar ratio of 0.7, 1.1 and 1.5 (first section in Table 1), i.e. defect, near stoichiometric and excess of citrate for the stoichiometric reaction with nitrates, respectively. As can be observed in Table 1, surface area is penalized ($5.1 \text{ m}^2 \text{ g}^{-1}$) for low CA/N ratios due to a rapid rate of reaction during combustion, or abrupt weight loss as determined by TGA (Fig. S1), which causes an important temperature increase and promotes crystal growth (51 nm). A more progressive combustion obtained with 1.1 CA/N ratio increases surface area up to $10.6 \text{ m}^2 \text{ g}^{-1}$ while limits crystal size (40 nm) and phase segregations (Fig. S2). However, this trend is not observed for perovskites prepared with higher CA/N ratios, leading to a surface area of $10.1 \text{ m}^2 \text{ g}^{-1}$ and a crystal size of 67 nm (CA/N = 1.5). More details can be found in the supplementary material.

The influence of the pH of the gel was also studied during the synthesis procedure of LaCoO_3 crystalline structure. Six perovskites were prepared adjusting the pH of the gel to 3, 4.5, 6, 7, 8 and 9 by ammonia addition LCO (1.1/3, 4.5, 6, 7, 8 or 9/700). Almost irrelevant influence in XRD patterns (not shown) as well as in textural properties is observed (second section in [Table 1](#)).

Finally, the influence of the calcination protocol was studied by calcining perovskites gels at 600, 700, 800 and 900 °C (LCO (1.1/7/600, 700, 800 or 900), third section in [Table 1](#)). Pure perovskite phase with no impurities or segregation was observed by XRD (Fig. S3) for calcination temperatures above 700 °C. On the contrary, the sample calcined at 600 °C presented characteristic diffraction peaks attributed to $\text{La}(\text{OH})_3$ along with those corresponding to perovskite. As could be expected, inversely proportional relation was observed between crystal size and surface area. The highest surface area ($14.6 \text{ m}^2 \text{ g}^{-1}$) corresponds to the smallest crystal size (24 nm) for a calcination temperature of 600 °C whereas the lowest surface area ($4.3 \text{ m}^2 \text{ g}^{-1}$) corresponds to the larger crystal size (212 nm) for a calcination temperature of 900 °C ([Table 1](#)). No significant differences were observed in the samples apart from a displacement to lower temperatures of reduction peaks with lower calcinations temperatures (Fig. S4).

[Fig. 1](#) shows the NO-to- NO_2 conversion (Eq. (1)) with increasing temperature for the prepared LaCoO_3 perovskites. The equilibrium conversion for the studied gas stream-feed composition (650 ppm NO, 6% O₂ and Ar to balance) with temperature is also included in broken line as a reference. Differences in the catalytic behavior for the NO-to- NO_2 oxidation among prepared perovskites can be almost exclusively linked to the surface area and the presence/absence of impurities, as no significant differences have been observed by other characterization techniques such as H₂-TPR (Fig. S4). Qualitatively, similar trends of NO conversion have been observed for all prepared samples, i.e. increasing NO conversion due to the promotion of oxidation kinetic constant with temperature, maximum NO conversion at intermediate temperatures and decreasing NO conversion in a thermodynamically controlled regime due to the exothermicity of the reaction. As can be observed in [Fig. 1a](#), NO conversion with LCO (0.7/7/700), resulted in significantly lower values in the whole temperature range with respect to its counterparts LCO (1.1/7/700) and LCO (1.5/7/700), prepared with higher citric acid to nitrates molar ratios (CA/N). NO conversion penalization was directly linked to lower surface area and the presence of segregated phases such as cobalt oxide (Co_3O_4), lanthanum oxide (La_2O_3) and lanthanum hydroxide ($\text{La}(\text{OH})_3$), as revealed by XRD (Fig. S2). [Fig. 1b](#) shows that irrespective of the pH of the gel the NO conversion of the resultant perovskites was almost similar, in agreement with similar surface area values and

the absence of impurities already reported. Finally, [Fig. 1c](#) makes evident that a calcination temperature of 700 °C promotes NO conversion, achieving a maximum value of 77% at 300–350 °C. NO conversion is penalized for lower and higher calcination temperatures, due to the presence of impurities and surface area diminution, respectively.

In summary, optimum preparation procedure of LaCoO_3 perovskites requires near stoichiometric citrate to nitrate ratio in the starting solution for a progressive decomposition, a pH of the gel of 8 (although its impact is almost irrelevant) and calcination temperatures of 700 °C in order to avoid impurities but with low surface area penalization. Finally, it was also observed that the calcination procedure also affects the physico-chemical properties of the perovskites. LCO (1.1/9/700) sample, calcined in a fixed bed reactor with 60 mL min^{-1} of 5% O₂/He gas stream, increases the surface area ($15.2 \text{ m}^2 \text{ g}^{-1}$) with respect to LCO (1.1/9/700) sample ($13.2 \text{ m}^2 \text{ g}^{-1}$) calcined in static air. This could be related to a higher capacity to purge released gases and remove excess reaction heat avoiding hot spots and limiting crystal growth. Thus, for Sr doped perovskites preparations calcinations in fixed bed reactor with 60 mL min^{-1} 5% O₂/He gas stream was defined as the standard calcination protocol.

A similar study was performed with LaMnO_3 perovskites determining that optimum preparation procedure involves the formula LMO (1.1/6/600), i.e. i) near stoichiometric citrate to nitrate molar ratio (CA/N = 1.1), similar to LaCoO_3 perovskite; ii) pH value of the gel adjusted to 6. As opposite to LaCoO_3 perovskites, the pH of the gel has a notable impact in the specific surface area and crystal size ([Table 1](#)) of the prepared solids; iii) calcination temperature of 600 °C, it was possible to decrease calcination temperature with respect to LaCoO_3 perovskites without presence of impurities.

Thus, it can be concluded that optimal preparation conditions for LaMnO_3 differ from those reported previously by Dong et al. [22]. On the one hand, the effect of the pH of the precursor solution for Mn perovskites is confirmed, although the calcination temperature can be significantly decreased. On the other hand, in the present study, the optimum pH value of the solution precursor results in 6 instead of pH = 8 reported by Dong et al. [22].

The oxidation capacity of NO-to- NO_2 of LaCoO_3 and LaMnO_3 perovskites prepared by optimum procedure, can be observed in [Fig. 2](#). LaMnO_3 perovskite presented higher NO conversion with respect to LaCoO_3 at low temperature ($T < 250$ °C), in line with higher exposed surface area of LaMnO_3 ($26.0 \text{ m}^2 \text{ g}^{-1}$) with respect to LaCoO_3 ($11.0 \text{ m}^2 \text{ g}^{-1}$). However, at higher temperature ($T > 250$ °C) similar or even slightly higher NO conversion is observed for LaCoO_3 perovskite, suggesting higher intrinsic activity in comparison to LaMnO_3 . For temperatures higher than 325 °C, the

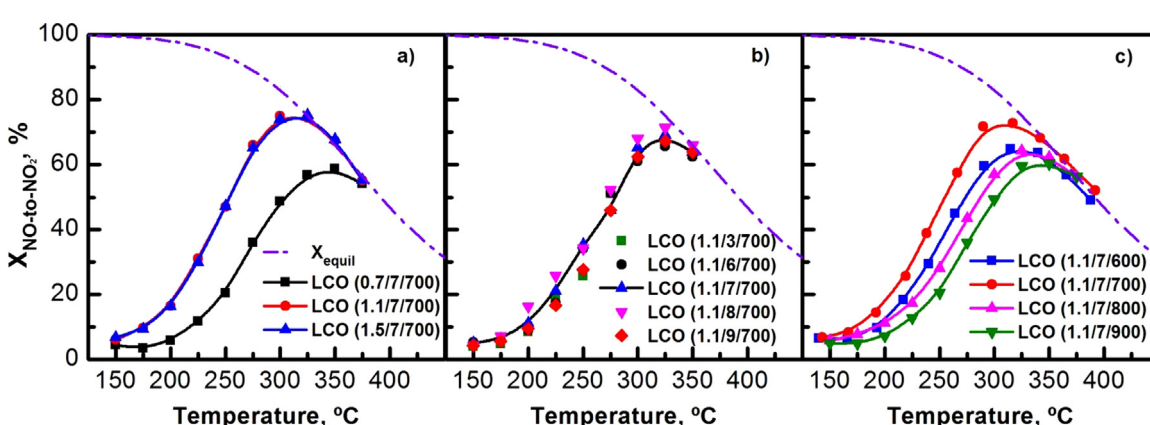


Fig. 1. NO-to- NO_2 oxidation capacity of LaCoO_3 perovskites prepared with different synthesis conditions: (a) citric acid to nitrate molar ratios (CA/N = 0.7, 1.1 and 1.5), (b) pH values of the gel (pH = 3, 6, 7, 8 and 9) and (c) calcination temperature (Temp. = 600, 700, 800, 900 °C).

Table 2

NO-to- NO_2 oxidation conversions and reaction rates of LaMnO_3 and LaCoO_3 perovskites in a differential reactor.

LaCoO_3 (LCO 1.1/8/700 5% O ₂ /He)			LaMnO_3 (LMO 1.1/6/600 5% O ₂ /He)		
Temperature, °C	$X_{\text{NO-to-NO}_2}$, %	($-r_A$), $\mu\text{mol min}^{-1} \text{m}^{-2}$	Temperature, °C	$X_{\text{NO-to-NO}_2}$, %	($-r_A$), $\mu\text{mol min}^{-1} \text{m}^{-2}$
140	2.64	0.260	140	5.74	0.281
164	3.72	0.367	163	5.85	0.286
188	7.56	0.746	189	8.10	0.396
211	14.57	1.437	218	12.71	0.621
236	25.65	2.531	238	19.01	0.929

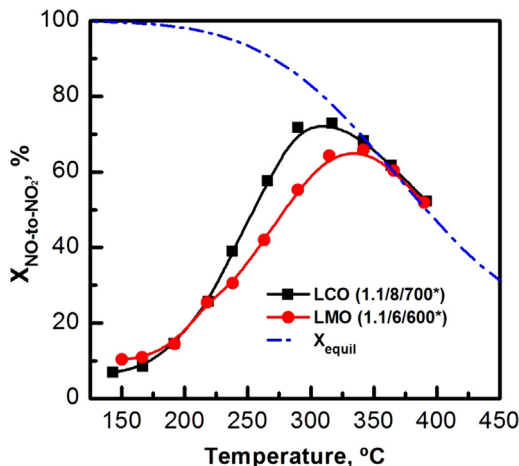


Fig. 2. NO-to- NO_2 oxidation capacity of LaCoO_3 and LaMnO_3 perovskites prepared by optimal synthesis conditions.

activity of both catalysts decreased in line with the thermodynamic equilibrium.

A kinetic study performed under differential reactor conditions ($X_A < 15\%$) in the absence of mass transfer limitations (total flow rate $> 1500 \text{ mL min}^{-1}$ and particle size $< 0.5 \text{ mm}$, Fig. S5) allowed us calculating reaction rates normalized to exposed surface area unit ($\mu\text{mol m}^{-2} \text{ min}^{-1}$). Table 2 confirms higher intrinsic activity of LaCoO_3 with respect to LaMnO_3 . The activation energy for the NO oxidation reaction over LaMnO_3 and LaCoO_3 perovskites are determined from Fig. 3, which represents a logarithmic plot of the reaction rate as a function of the inverse of temperature. Apparent activation energies result in 33.7 and 49.7 kJ mol⁻¹ for LMO (1.1/6/600 in 5% O₂/He) and LCO (1.1/8/700 in 5% O₂/He), respec-

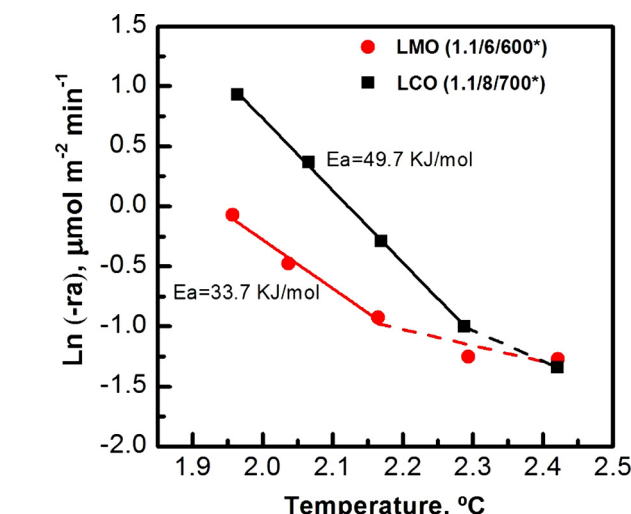


Fig. 3. Linearization of Arrhenius equation in order to obtain activation energies of NO-to- NO_2 reaction over LaCoO_3 and LaMnO_3 perovskites.

Table 3

Textural properties of $\text{La}_{1-x}\text{Sr}_x\text{CoO}_3$ and $\text{La}_{1-x}\text{Sr}_x\text{MnO}_3$ perovskites, with x from 0 to 0.5.

Sample	Surface area, $\text{m}^2 \text{ g}^{-1}$	V_p , $\text{cm}^3 \text{ g}^{-1}$	d_c , nm
LaCoO_3 ^a	16.2	0.09	32
$\text{La}_{0.9}\text{Sr}_{0.1}\text{CoO}_3$ ^a	17.2	0.09	27
$\text{La}_{0.8}\text{Sr}_{0.2}\text{CoO}_3$ ^a	21.4	0.11	18
$\text{La}_{0.7}\text{Sr}_{0.3}\text{CoO}_3$ ^a	20.3	0.12	18
$\text{La}_{0.6}\text{Sr}_{0.4}\text{CoO}_3$ ^a	18.8	0.11	16
$\text{La}_{0.5}\text{Sr}_{0.5}\text{CoO}_3$ ^a	15.7	0.09	15
LaMnO_3 ^b	28.2	0.14	27
$\text{La}_{0.9}\text{Sr}_{0.1}\text{MnO}_3$ ^b	33.1	0.17	21
$\text{La}_{0.8}\text{Sr}_{0.2}\text{MnO}_3$ ^b	35.8	0.18	20
$\text{La}_{0.7}\text{Sr}_{0.3}\text{MnO}_3$ ^b	39.1	0.17	15
$\text{La}_{0.6}\text{Sr}_{0.4}\text{MnO}_3$ ^b	47.9	0.19	15
$\text{La}_{0.5}\text{Sr}_{0.5}\text{MnO}_3$ ^b	39.6	0.16	14

^a All samples synthesized under same conditions that LCO (1.1/8/700).

^b All samples synthesized under same conditions that LMO (1.1/6/600).

tively, except for lower temperatures (broken lines) suggesting probably that at so lower temperatures (below 190 °C for LMO and 165 °C for LMO) external diffusion could not be completely ruled out. Chen et al. [14] reported a value of $44.8 \pm 2.7 \text{ kJ mol}^{-1}$ for La_xMnO_3 ($0.9 < x < 1.1$) in the range 200–275 °C and Qi et al. [31] a value of 31.0 kJ mol^{-1} for LaMnO_3 in the range 175–225 °C. For LaCoO_3 , Choi et al. [32] found 55.4 kJ mol^{-1} for LaCoO_3 perovskite between 190 and 220 °C.

3.2. Strontium doped LaCoO_3 and LaMnO_3 perovskites

The cations in the perovskite lattice can be partially replaced by foreign cations with no large change in crystalline structure, producing substituted perovskites, i.e. $\text{A}_{1-x}\text{A}'_x\text{BO}_3$ or $\text{AB}_{1-x}\text{B}'_x\text{O}_3$. This property has frequently been exploited in catalysis because the substitution of foreign cations in A and/or B sites usually promotes catalytic activity [10].

In order to determine the influence of strontium doping, $\text{La}_{1-x}\text{Sr}_x\text{BO}_3$ perovskites (B=Mn or Co) were synthesized with La substitutions $x=0, 0.1, 0.2, 0.3, 0.4$ and 0.5, using $\text{Sr}(\text{NO}_3)_2$ as precursor, and the optimum synthesis procedure determined in the previous section.

3.2.1. X-ray diffraction (XRD)

Fig. 4 shows the XRD patterns of the prepared $\text{La}_{1-x}\text{Sr}_x\text{CoO}_3$ (Fig. 4a) and $\text{La}_{1-x}\text{Sr}_x\text{MnO}_3$ (Fig. 4b) perovskites. Pure perovskite diffraction patterns were obtained for low Sr substitution degrees, in the absence of impurities. However, phase segregation in the form of Co_3O_4 , $\text{La}(\text{OH})_3$ and SrCO_3 start to be detectable by XRD for $\text{La}_{0.6}\text{Sr}_{0.4}\text{CoO}_3$ perovskite, and become even more significant for $\text{La}_{0.5}\text{Sr}_{0.5}\text{CoO}_3$. On the other hand, in the case of Mn-based perovskites, the presence of impurities in the form of SrCO_3 was only evident for the highest Sr substituted sample, i.e. $\text{La}_{0.5}\text{Mn}_{0.5}\text{CoO}_3$. Thus, it can be concluded that LaMnO_3 perovskites allow higher Sr accommodation in the lattice without phase segregation in comparison to LaCoO_3 perovskites.

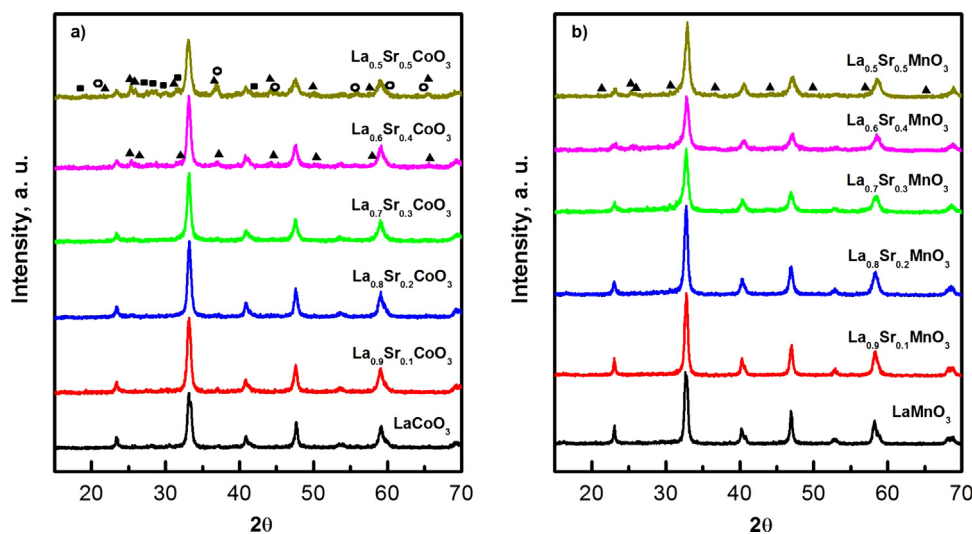


Fig. 4. XRD diffractograms of (a) $\text{La}_{1-x} \text{Sr}_x \text{CoO}_3$ and (b) $\text{La}_{1-x} \text{Sr}_x \text{MnO}_3$ with x ranging from 0 to 0.5 (\blacktriangle SrCO_3 , \blacksquare La(OH)_3 and \circlearrowleft Co_3O_4).

Table 4

Deconvoluted hydrogen consumption related to different reduction steps for $\text{La}_{1-x} \text{Sr}_x \text{CoO}_3$ perovskites, with x from 0 to 0.5.

Sample	H_2/Co	$\text{O}_2 \text{chem}^{\text{a}}$, $\mu\text{mol H}_2 \text{g}^{-1}$	$\text{Co}^{3+} \rightarrow \text{Co}^{2+}{}^{\text{b}}$, $\mu\text{mol H}_2 \text{g}^{-1}$	$\text{Co}^{2+} \rightarrow \text{Co}^0{}^{\text{c}}$, $\mu\text{mol H}_2 \text{g}^{-1}$	$\text{Co}^{3+}/\text{Co}^{\text{d}}$
LaCoO_3	1.53	136.33	2019.23	3938.58	0.98
$\text{La}_{0.9}\text{Sr}_{0.1}\text{CoO}_3$	1.55	360.17	2012.11	4142.19	1.03
$\text{La}_{0.8}\text{Sr}_{0.2}\text{CoO}_3$	1.53	404.02	2085.18	4230.39	1.01
$\text{La}_{0.7}\text{Sr}_{0.3}\text{CoO}_3$	1.49	627.78	2038.51	3985.23	0.98
$\text{La}_{0.6}\text{Sr}_{0.4}\text{CoO}_3$	1.38	578.98	1984.67	2438.72	0.61
$\text{La}_{0.5}\text{Sr}_{0.5}\text{CoO}_3$	1.34	611.33	1879.61	2253.11	0.60

^a Integration of peak centered around 225 °C.

^b Integration of peaks centered around 350 °C.

^c Sum of integrated peaks centered around 500, 575 and 650 °C.

^d Estimation of relative Co^{3+} content based on deconvoluted peak areas relation, $\text{Co}^{3+}/\text{Co} = (\text{Co}^{3+} \rightarrow \text{Co}^{2+})/(\text{Co}^{2+} \rightarrow \text{Co}^0)/2$.

Irrespective of B cation, Mn or Co, increasing Sr substitution degree leads to a widening of the diffraction peaks (Fig. S6) due to smaller crystal size of the solids, which has been quantified by Scherrer's equation (Table 3). In fact, the largest crystal size, 32 and 27 nm, is detected for the non-substituted LaCoO_3 and LaMnO_3 samples, respectively, and the smallest, 15 and 14 nm, for the highest substitution degree $\text{La}_{0.5}\text{Sr}_{0.5}\text{CoO}_3$ and $\text{La}_{0.5}\text{Sr}_{0.5}\text{MnO}_3$, respectively.

Furthermore, the intensity decrease of the diffraction peaks with the displacement towards higher diffraction angles by Sr doping, suggests that La^{3+} cations were successfully substituted by Co^{3+} or by $\text{Mn}^{3+}/\text{Mn}^{4+}$ in the perovskite lattice structure. In addition, gradual changes in the characteristic pattern are observed from rhombohedral LaCoO_3 (PDF number: 048-0123) and $\text{La}_{0.88}\text{MnO}_{2.91}$ (PDF number: 089-0679) to rhombohedral distorted $\text{La}_{0.5}\text{Sr}_{0.5}\text{CoO}_{2.91}$ (PDF number: 048-0122) and rhombohedral $\text{La}_{0.5}\text{Sr}_{0.5}\text{MnO}_3$ (PDF number: 048-0122), respectively [10,33–35].

3.2.2. Textural properties

The influence of Sr content on textural properties was studied by N_2 adsorption-desorption at low temperature (Table 3). The evolution of the specific surface area (SSA) with respect to the substitution degree reveals a maximum for $\text{La}_{0.8}\text{Sr}_{0.2}\text{CoO}_3$ and $\text{La}_{0.6}\text{Sr}_{0.4}\text{MnO}_3$, samples. The SSA is enhanced by 32% for $\text{La}_{0.8}\text{Sr}_{0.2}\text{CoO}_3$ ($21.4 \text{ m}^2 \text{ g}^{-1}$) with respect to the non-substituted sample ($16.2 \text{ m}^2 \text{ g}^{-1}$) whereas the SSA enhancement was notably higher (70%) for $\text{La}_{0.6}\text{Sr}_{0.4}\text{MnO}_3$ ($47.9 \text{ m}^2 \text{ g}^{-1}$) in comparison to the non-substituted sample ($28.2 \text{ m}^2 \text{ g}^{-1}$). The SSA development for Sr substituted samples can be directly linked to the lower crystal

size of the samples, as it was revealed by XRD (Table 3). Although crystal size was further decreased for higher Sr substitution, SSA was penalized, which was attributed to the presence of phase segregations that may block the access to the pores [26]. Note that this SSA penalization resulted evident for Sr substitutions higher than 0.3 and 0.4 for LaCoO_3 and LaMnO_3 perovskites, respectively, which again is a clear evidence of the higher ability of LaMnO_3 to accommodate Sr in the lattice with no phase segregation, and thus allowing higher promotion effect on textural properties due to Sr incorporation.

3.2.3. Reducibility (H_2 -TPR)

It has been found that the catalytic activities of lanthanum perovskites were mainly determined by the B site element properties [20]. In this sense, the redox properties of Mn and Co-based perovskites were investigated by H_2 -TPR experiments. Fig. 5 illustrates the H_2 -TPR for $\text{La}_{1-x}\text{Sr}_x\text{CoO}_3$ samples, where two main H_2 consumption regions can be distinguished, i.e. below and above 500 °C. Hydrogen consumption below 500 °C can be deconvoluted into two different contributions centered around 225 and 350 °C, which are assigned to the reduction of quimisorbed oxygen in the catalyst surface and the progressive reduction of Co^{3+} to Co^{2+} from the surface to the inner layers with increasing temperature, respectively, maintaining the perovskite structure,



On the other hand, hydrogen consumption above 500 °C can be assigned to the final reduction of Co^{2+} to Co^0 which is accomplished in two different consumption peaks attributed to superficial

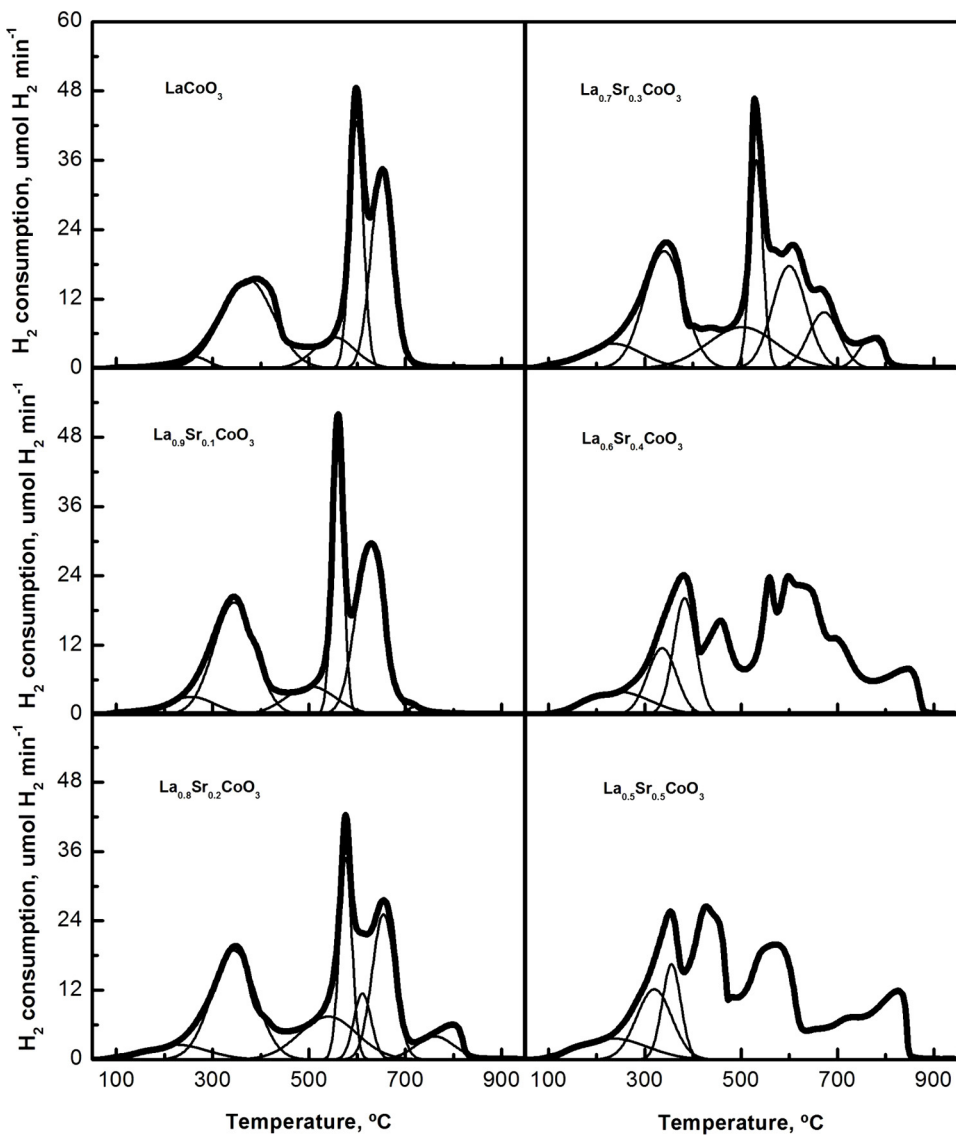
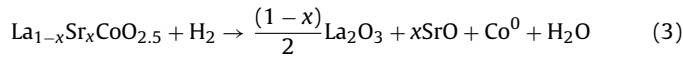


Fig. 5. H_2 -TPR profiles of $\text{La}_{1-x}\text{Sr}_x\text{CoO}_3$ samples with x ranging from 0 to 0.5.

and bulk reduction, resulting in the destruction of the perovskite structure,



The aforementioned reduction peaks can be clearly observed for perovskite samples with low Sr substitution up to $\text{La}_{0.7}\text{Sr}_{0.3}\text{CoO}_3$. In contrast, reduction peak assignation is not straightforward for higher Sr substitution degree samples. In those cases, an additional reduction peak can be observed at higher temperature (800°C) which is not related with hydrogen consumption but instead is ascribed to surface decomposition of residual carbonates in the form of CO_2 which alters the TCD signal, as detected by MS [26,36]. As a general trend, it can be observed that increasing Sr content results in the displacement of reduction peaks to lower temperature, related with increasing BET surface area (SSA) which promotes sample reducibility.

Focusing on low Sr substituted samples, the total hydrogen consumption related to the total amount of cobalt in the sample (Table 4) can be used to estimate the mean oxidation state of cobalt. Perovskite reduction stoichiometry (Eqs. (2) and (3)) reveals that 1.5 mol of H_2 is needed to reduce 1 mol of Co^{3+} to Co^0 . Calculated H_2/Co ratios are in all cases close to 1.5, this confirming an oxida-

tion state of Co^{3+} in the initial perovskite and discard the presence of Co^{4+} . Consequently, it can be deduced that generation of oxygen vacancies is the only mechanism available to accomplish charge compensation in LaCoO_3 perovskites when strontium is doped into the structure. In fact, increasing H_2 consumption due to reduction of chemisorbed oxygen in surface vacancies was observed with increasing Sr doping (Table 4), reaching this contribution about 5 times for $\text{La}_{0.7}\text{Sr}_{0.3}\text{CoO}_3$ with respect to non-substituted LaCoO_3 perovskite. Furthermore, it was experimentally verified that the amount of hydrogen consumed in the reduction of $\text{Co}^{3+} \rightarrow \text{Co}^{2+}$ was half of that consumed for the reduction of $\text{Co}^{2+} \rightarrow \text{Co}^0$, which validates the peak deconvolution assignments. Co^{3+} relative content with respect to total cobalt in the sample was calculated from deconvoluted peaks areas relation, i.e. dividing the H_2 consumption related to $\text{Co}^{3+} \rightarrow \text{Co}^{2+}$ reduction by half the H_2 consumption related to $\text{Co}^{2+} \rightarrow \text{Co}^0$ reduction. It can be observed that cobalt exists only in the 3+ oxidation state in the perovskite lattice for low Sr substituted samples. On the contrary, for high Sr substituted samples ($\text{La}_{0.6}\text{Sr}_{0.4}\text{CoO}_3$ and $\text{La}_{0.5}\text{Sr}_{0.5}\text{CoO}_3$) lower Co^{3+}/Co ratios were observed. This fact can be explained by the presence of a significant amount of cobalt as Co_3O_4 (not included when calculating H_2 consumption to reduce Co^{3+} to Co^0), as observed by

Table 5

Deconvoluted hydrogen consumption related to different reduction steps for $\text{La}_{1-x}\text{Sr}_x\text{MnO}_3$ perovskites, with x from 0 to 0.5.

Sample	H_2/Mn	$\text{O}_{\text{chem}}^{\text{a}}$, $\mu\text{mol H}_2 \text{g}^{-1}$	$\text{Mn}^{4+} \rightarrow \text{Mn}^{3+}$ ^b , $\mu\text{mol H}_2 \text{g}^{-1}$	$\text{Mn}^{3+} \rightarrow \text{Mn}^{2+}$ (superficial) ^c , $\mu\text{mol H}_2 \text{g}^{-1}$	$\text{Mn}^{3+} \rightarrow \text{Mn}^{2+}$ (bulk) ^d , $\mu\text{mol H}_2 \text{g}^{-1}$	$\text{Mn}^{4+}/\text{Mn}^{\text{e}}$
LaMnO_3	0.80	148	724	606	1967	0.28
$\text{La}_{0.9}\text{Sr}_{0.1}\text{MnO}_3$	0.70	155	522	707	1746	0.21
$\text{La}_{0.8}\text{Sr}_{0.2}\text{MnO}_3$	0.70	142	642	908	1492	0.27
$\text{La}_{0.7}\text{Sr}_{0.3}\text{MnO}_3$	0.71	158	879	1099	1002	0.42
$\text{La}_{0.6}\text{Sr}_{0.4}\text{MnO}_3$	0.65	135	913	815	1151	0.43
$\text{La}_{0.5}\text{Sr}_{0.5}\text{MnO}_3$	0.70	194	990	1022	1204	0.44

^a Integration of peak centered around 175 °C.

^b Integrated peak centered around 300 °C.

^c Integrated peak centered around 425 °C.

^d Sum of integrated peaks centered around 600, 750 and 825 °C.

^e Estimation of relative Mn^{4+} content based on deconvoluted peak areas relation. $\text{Mn}^{4+}/\text{Mn} = (\text{Mn}^{4+} \rightarrow \text{Mn}^{3+})/(\text{Mn}^{3+} \rightarrow \text{Mn}^{2+}$, superficial + bulk).

Table 6

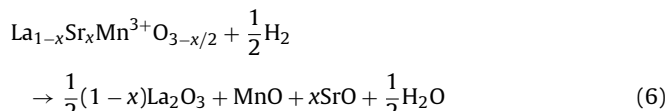
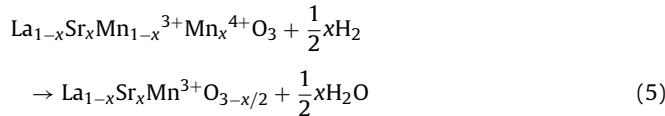
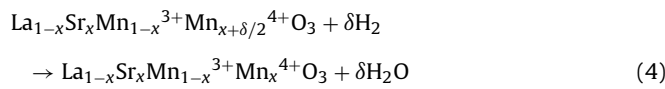
Surface atomic ratios of different compounds in $\text{La}_{1-x}\text{Sr}_x\text{CoO}_3$ and $\text{La}_{1-x}\text{Sr}_x\text{MnO}_3$ perovskites with x from 0 to 0.5.

Sample	$\text{Sr}/(\text{Co or Mn})$	$\text{La}/(\text{Co or Mn})$	$\text{Sr}_{\text{segregated}}/\text{Sr}_{\text{total}}$	$\text{O}_{\text{lattice}}/\text{O}_{\text{total}}$
LaCoO_3	0.00 (0.00)	2.00 (1.00)	–	0.41
$\text{La}_{0.9}\text{Sr}_{0.1}\text{CoO}_3$	0.34 (0.10)	1.54 (0.90)	0.56	0.41
$\text{La}_{0.8}\text{Sr}_{0.2}\text{CoO}_3$	0.52 (0.20)	1.43 (0.80)	0.63	0.36
$\text{La}_{0.7}\text{Sr}_{0.3}\text{CoO}_3$	0.68 (0.30)	1.37 (0.70)	0.72	0.32
$\text{La}_{0.6}\text{Sr}_{0.4}\text{CoO}_3$	0.70 (0.40)	0.78 (0.60)	0.75	0.35
$\text{La}_{0.5}\text{Sr}_{0.5}\text{CoO}_3$	1.13 (0.50)	0.82 (0.50)	0.84	0.28
LaMnO_3	0.00 (0.00)	1.40 (1.00)	–	0.52
$\text{La}_{0.9}\text{Sr}_{0.1}\text{MnO}_3$	0.23 (0.10)	1.38 (0.90)	0.35	0.49
$\text{La}_{0.8}\text{Sr}_{0.2}\text{MnO}_3$	0.40 (0.20)	1.36 (0.80)	0.33	0.46
$\text{La}_{0.7}\text{Sr}_{0.3}\text{MnO}_3$	0.52 (0.30)	0.85 (0.70)	0.34	0.48
$\text{La}_{0.6}\text{Sr}_{0.4}\text{MnO}_3$	0.62 (0.40)	0.84 (0.60)	0.35	0.44
$\text{La}_{0.5}\text{Sr}_{0.5}\text{MnO}_3$	0.82 (0.50)	0.68 (0.50)	0.34	0.44

In brackets are shown theoretical values based on nominal composition.

XRD. The presence of a well dispersed Co_3O_4 phase also induces some changes in the H_2 -TPR experiments. In fact, the dispersed cobalt oxide is reduced around 200 °C, increasing the peak previously assigned to the reduction of quimisorbed oxygen on the surface.

Fig. 6 shows TPR profiles of Mn perovskites, all curves exhibiting similar shapes with two main reduction peaks, below and above 550 °C. H_2 consumption below 550 °C was deconvoluted into three contributions located at 175, 300 and 425 °C, which are ascribed to the reduction of nonstoichiometric excess oxygen accommodated within the lattice, reduction of Mn^{4+} to Mn^{3+} and reduction of Mn^{3+} to Mn^{2+} located in a coordination unsaturated microenvironment [22,37,38], respectively. Theoretically, same contents of Sr^{2+} and Mn^{4+} are expected in the perovskite structure in order to accomplish charge balance. Furthermore, it has been reported that even stoichiometric LaMnO_3 perovskites can show mixed $\text{Mn}^{3+}/\text{Mn}^{4+}$ oxidation state balanced by excess oxygen in the lattice. Thus, reduction sequence of $\text{La}_{1-x}\text{Sr}_x\text{MnO}_3$ perovskites can be written as:



where x represents the Sr molar fraction and δ the excess of oxygen accommodated within the lattice. On the other hand, H_2 consumption above 550 °C was attributed to bulk reduction of

Mn^{3+} to Mn^{2+} and destruction of the perovskite. As previously observed for LaCoO_3 perovskites, an additional peak was observed at higher temperature (800 °C) for high Sr substituted samples due to SrCO_3 decomposition.

Total H_2 consumption related to Mn content in the sample (H_2/Mn) is indicative of an average Mn oxidation state. 1 mol of H_2 is needed to reduce 1 mol of Mn^{4+} to Mn^{2+} whereas 0.5 moles of H_2 is needed to reduce 1 mol of Mn^{3+} to Mn^{2+} . Calculated H_2/Mn ratios resulted in between 0.5 and 1 for all samples, revealing a hybrid $\text{Mn}^{4+}/\text{Mn}^{3+}$ oxidation state (Table 5). Observing numerical values of deconvoluted and integrated signals, it can be observed that H_2 consumption related to reduction of oxygen excess is maintained fairly constant with Sr doping. The observed increasing amount of H_2 consumption is attributed to reduction of Mn^{4+} to Mn^{3+} , revealing that Sr doping promotes the presence of Mn^{4+} in the perovskite structure to compensate the charge imbalance produced by Sr. A similar trend observed for H_2 consumption is assigned to superficial reduction of Mn^{3+} to Mn^{2+} , which correlates adequately with increasing surface area of the samples. Reduction of bulk Mn^{3+} to Mn^{2+} is complementary to surface Mn^{3+} to Mn^{2+} reduction. Thus, H_2 consumption related to bulk reduction of Mn^{3+} to Mn^{2+} decrease with Sr doping. Mn^{4+} content determined from integrated H_2 consumption of deconvoluted signals show, as a general trend, an increasing content of Mn^{4+} with increasing Sr doping, obtaining almost 50% of manganese as Mn^{4+} for high Sr doped perovskites.

As a general trend it can be observed that increasing Sr content results in a displacement of reduction peaks to lower temperature, related with an increasing BET surface area (SSA) which promotes sample reducibility, as it was observed for LaCoO_3 perovskites.

3.2.4. Concentration and strength of the oxygen species (O_2 -TPD)

Partial substitution of La^{3+} by Sr^{2+} can modify Co or Mn oxidation state as previously observed by H_2 -TPR, but oxygen vacancies can be also promoted in order to accomplished charge compensation.

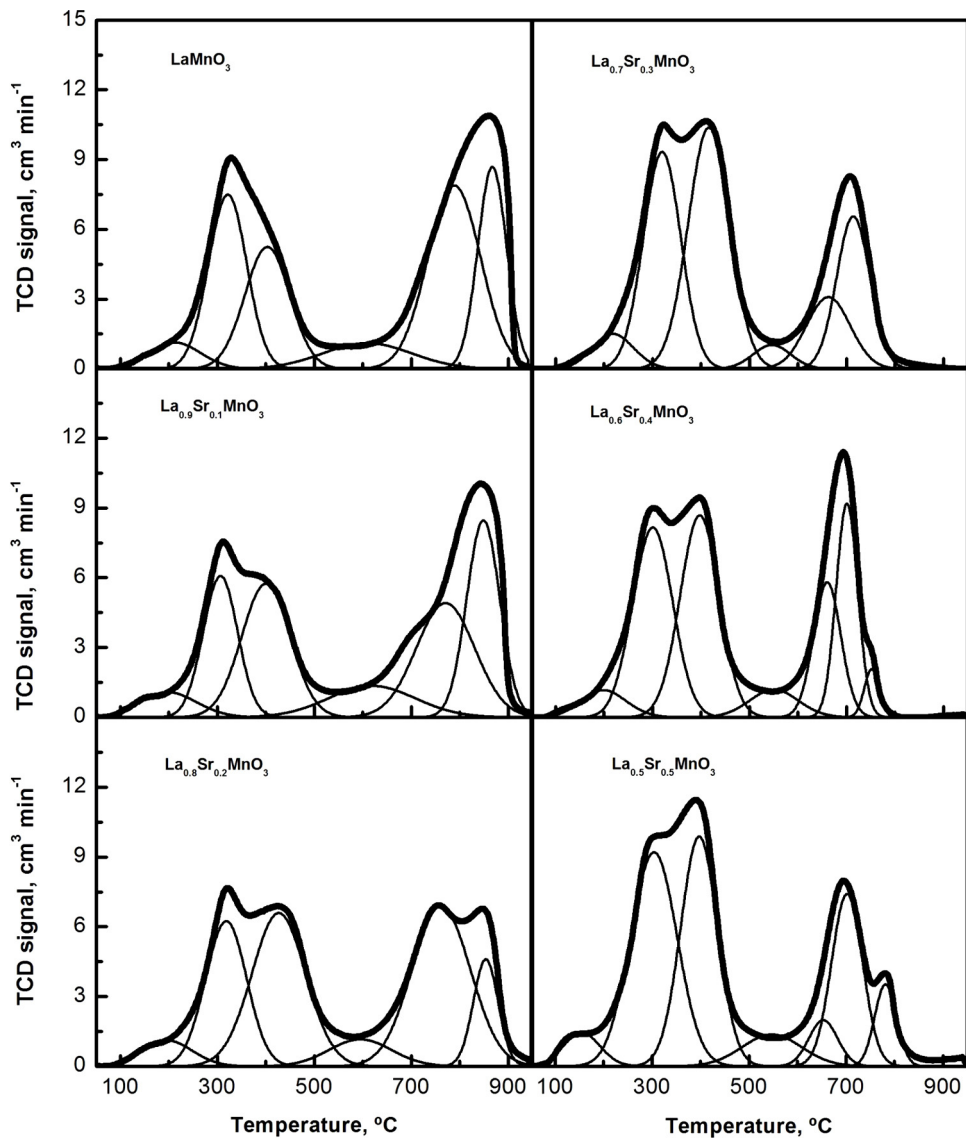


Fig. 6. H_2 -TPR profiles of $\text{La}_{1-x}\text{Sr}_x\text{MnO}_3$ samples with x ranging from 0 to 0.5.

Table 7

NO-to- NO_2 oxidation activity of different perovskite formulations reported in the literature, under different reaction conditions, in comparison to $\text{La}_{1-x}\text{Sr}_x\text{MnO}_3$ and $\text{La}_{1-x}\text{Sr}_x\text{CoO}_3$ prepared in this work.

Type	Formulation	Shape	Feedstream	GHSV, h^{-1}	$T, ^\circ\text{C}$	$X_{\text{NO-to-NO}_2}, \%$	Reference
Co-based perovskites	LaCoO_3	Powder	[NO] = 100 ppm; $[\text{O}_2]$ = 10%	30,000	260	83.0	Chen et al. [11]
	$\text{La}_{0.9}\text{Sr}_{0.1}\text{CoO}_3$	Monolith	[NO] = 400 ppm; $[\text{O}_2]$ = 8%	30,000	300	86.0	Kim et al. [25]
	$\text{La}_{0.7}\text{Sr}_{0.3}\text{CoO}_3$	Powder	[NO] = 800 ppm; $[\text{O}_2]$ = 5%	80,000	300	74.1	Li et al. [26]
	$\text{La}_{0.7}\text{Sr}_{0.3}\text{Co}_{0.8}\text{Fe}_{0.2}\text{O}_3$	Powder	[NO] = 750 ppm; $[\text{O}_2]$ = 5%	80,000	300	84.6	Ma et al. [55]
	$\text{La}_{0.7}\text{Sr}_{0.3}\text{CoO}_3$	Powder	[NO] = 650 ppm; $[\text{O}_2]$ = 6%	123,500	300	82.5	This work
Mn-based perovskites	LaMnO_3	Monolith	[NO] = 400 ppm; $[\text{O}_2]$ = 8%	30,000	350	62.0	Qi et al. [31]
	$\text{La}_{0.9}\text{MnO}_3$	Powder	[NO] = 100 ppm; $[\text{O}_2]$ = 10% ^a	30,000	296	85.0	Chen et al. [14]
	$\text{La}_{0.9}\text{Sr}_{0.1}\text{MnO}_3$	Monolith	[NO] = 400 ppm; $[\text{O}_2]$ = 8%	30,000	350	62.5	Kim et al. [25]
	$\text{La}_{0.7}\text{Sr}_{0.3}\text{MnO}_3$	Powder	[NO] = 800 ppm; $[\text{O}_2]$ = 5%	80,000	350	70.2	Dong et al. [22]
	$\text{La}_{0.9}\text{Sr}_{0.1}\text{MnO}_3$	Powder	[NO] = 650 ppm; $[\text{O}_2]$ = 6%	123,500	350	64.9	This work

^a In the presence of H_2O and CO_2 .

In this sense, temperature programmed desorption of oxygen (O_2 -TPD) is a reliable technique to analyze the amount and the strength of adsorbed oxygen species. Fig. 7a and b shows the evolution of TCD signal obtained during O_2 -TPD experiments for $\text{La}_{1-x}\text{Sr}_x\text{CoO}_3$ and $\text{La}_{1-x}\text{Sr}_x\text{MnO}_3$ samples, respectively. The profiles clearly show two distinct regions where oxygen is desorbed, related to different O_2 species: the so-called α -oxygen (<550 °C) and β -oxygen (>550 °C)

[39]. α -Oxygen comprises weakly adsorbed species at the surface and lattice oxygen generated from the dislocations or grain frontiers [27]. Only the oxygen released from vacancies located very near to or on the surface is likely to desorb at this temperature. On the other hand, β -oxygen accounts for oxygen being released from inner layers of the lattice, which could cause the reduction of B site cation [27].

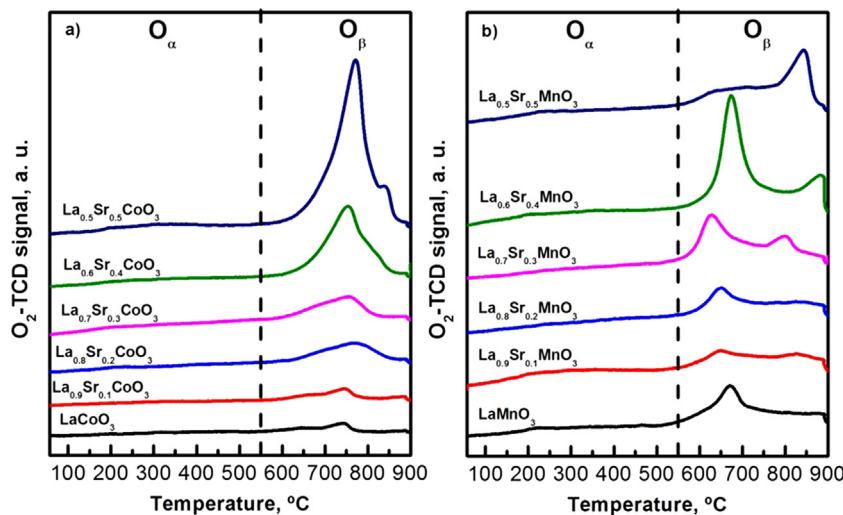


Fig. 7. O₂-TPD profiles of (a) La_{1-x}Sr_xCoO₃ and (b) La_{1-x}Sr_xMnO₃, with x ranging from 0 to 0.5 perovskites.

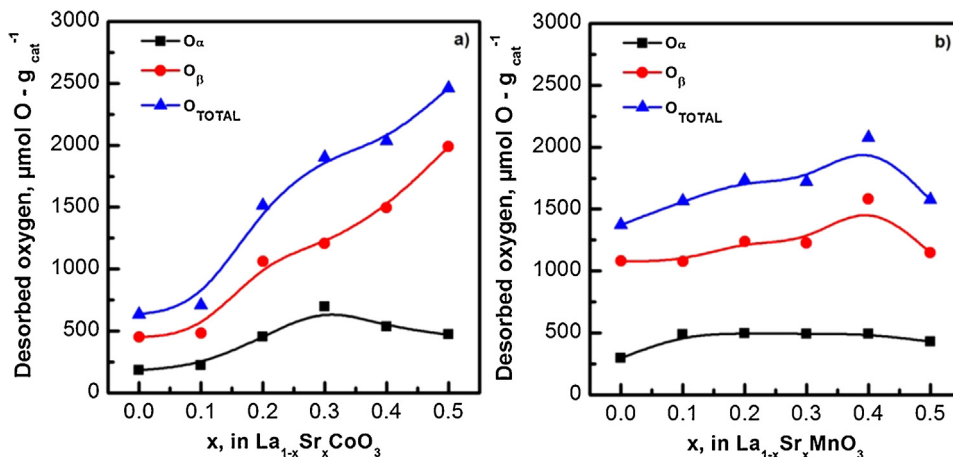


Fig. 8. Evolution of α , β and total desorbed oxygen species with substitution degree for: (a) La_{1-x}Sr_xCoO₃ and (b) La_{1-x}Sr_xMnO₃ perovskites.

Fig. 7a shows O₂-TPD profiles of La_{1-x}Sr_xCoO₃ samples and **Fig. 8a** the evolution of different oxygen species (O_α, O_β and O_{TOTAL}) with substitution degree. As already observed by H₂-TPR strontium doping does not induce any change in the cobalt oxidation state, and thus, the positive charge defect due to the substitution of La³⁺ by Sr²⁺ should be balanced by the formation of oxygen vacancies [33,40–44]. As can be observed, substitution degree up to 30%, i.e. La_{0.7}Sr_{0.3}CoO₃, nearly triples the amount of O_α species with respect to the non-substituted sample, which could be also related to the promotion of specific surface area [45]. On the contrary, substitution degrees higher than 0.4 penalize the amount of O_α species due to formation of surface impurities which reduce surface area. With respect to O_β, La substitution by Sr enhanced the formation of these species in the whole range. However, we verified by MS that TCD signal variations for temperatures higher than 600 °C were not only due to O₂ desorption but also due to CO₂ formation by surface carbonates decomposition. This explains the remarkable increase in the TCD signal at temperatures higher than 600 °C for perovskite samples with high substitution degree, as those samples presented high amount of surface impurities, as revealed by XRD.

La_{1-x}Sr_xMnO₃ samples (**Fig. 7b**) show the same desorption regions identified for Mn based samples attributed to O_α and O_β. However, strontium doping does not result in a significant change of O_α species in La_{1-x}Sr_xMnO₃ samples, as opposite to La_{1-x}Sr_xCoO₃ (**Fig. 8b**). Thus, charge compensation in La_{1-x}Sr_xMnO₃ samples

seems to be accomplished preferably by modification of Mn oxidation state (as observed by H₂-TPR) rather than formation of oxygen vacancies. In the high temperature region, the oxygen desorption peak situated around 600–700 °C is assigned to the release of lattice oxygen which results in the reduction of Mn⁴⁺ ions to Mn³⁺. This peak shifts to lower temperature and tends to increase as Sr substitution degree is increased, which suggests a higher facility of oxygen to diffuse along the lattice and a higher Mn⁴⁺ content [33]. It is worth to note that an additional peak appears around 800 °C for high Sr substituted samples which is assigned to the decomposition of surface impurities in the form of carbonates, mainly SrCO₃. Higher content of impurities changes the O₂ desorption profile for La_{0.5}Sr_{0.5}MnO₃.

3.2.5. Surface elemental composition and oxidation states (XPS)

X-ray photoelectron spectroscopy (XPS) is a surface-sensitive technique and provides information of the surface elemental composition and the oxidation state of each compound, which could be modified by Sr doping [44,46–48]. Surface composition and binding energies of La 3d_{5/2}, Co 2p_{3/2}, Sr 3d_{5/2} and O 1s core levels were recorded by XPS for LaCoO₃ perovskites (Fig. S7). La 3d_{5/2} transition was deconvoluted in two different contributions located at 832.9 and 834.6 eV with their corresponding shake up satellites. These contributions were assigned to La accommodated within the lattice and segregated lanthanum as an oxide (La₂O₃), respectively. Similar

behavior was observed for Sr 3d_{5/2} transition, fitting the observed spectra with two contributions located at 131.6 and 133.5 eV with their corresponding shake up satellites, and again assigned to contributions due to lattice and segregated strontium phases, mainly as SrCO₃, as observed by XRD. O 1s transition shows a broad emission line between 526 eV and 536 eV, which can be deconvoluted into three distinct peaks around 528.8, 531.2 and 534.0 eV. Lower BE value signal corresponds to lattice oxygen bonded to cations in the crystal structure (O²⁻_{latt}). Intermediate binding energy contribution (O_{ads}) is ascribed to O=C or O=C bonds, as for example in carbonates, oxygen bonded to cations as segregations (La₂O₃ or Co₃O₄) or weakly bonded O₂ (associated with surfaces defects, i.e. surface vacancies). The signal at highest binding energy values is due to water and hydroxyl groups on the surface [33,49–52]. Co 2p_{3/2} transition shows a strong asymmetric peak around 779.5 eV with a weak satellite peak at 790 eV. The former signal could be resolved into two components attributable to Co³⁺ (779.5 eV) and Co²⁺ (780.7) in a hybrid oxidation state environment, respectively. Besides, an additional contribution at 782.1 eV (with a shake-up satellite at 784.5) is needed in order to fit experimental data, which is assigned to Co²⁺ in a CoO segregated phase [37].

Table 6 presents Sr/Co and La/Co atomic surface ratios along with ratios of lattice oxygen and segregated strontium with respect to total oxygen and strontium content, respectively. As can be observed there is a surface enrichment of Sr and La irrespective of strontium doping degree, i.e. surface atomic ratio of strontium and La with respect to cobalt is notably higher than the theoretical value shown in brackets, which is in line with lanthanum and strontium segregates observed by XRD. On the other hand, it can be observed that segregated strontium fraction increases with increasing strontium doping degree, revealing a limited accommodation capacity of Sr in the La_{1-x}Sr_xCoO₃ lattice. With respect to O₂, decreasing contribution of lattice oxygen is detected in the O 1s transition as Sr doping increases, balanced with an increase contribution of oxygen adspecies or oxygen bonded to cations as segregations.

Similar procedure was followed with Sr doped LaMnO₃ perovskites, recording La 3d_{5/2}, Mn 2p_{3/2}, Sr 3d_{5/2} and O 1s transitions by XPS (Fig. S8). For these samples, it was possible to deconvolute La 3d_{5/2} transition in a unique component situated at 834.0 eV along with the shake-up satellite, assigned to lanthanum being part of the perovskite lattice. In contrast, as already observed for LaCoO₃ perovskites, two different components were needed to fit experimental Sr 3d_{5/2} transition, assigned to lattice and segregated strontium. Asymmetrical signal at 641.6 eV was recorded for Mn 2p_{3/2} transition with a weak satellite. Quantification of Mn oxidation state is rather difficult by XPS, due to small differences in the binding energy of Mn⁴⁺ and Mn³⁺ ions. Binding energy of Mn 2p_{3/2} transition appears near to the theoretical value attributed to Mn⁴⁺ and Mn³⁺, which is indicative of a mix oxidation state [10,33,49,53,54]. O 1s transition for La_{1-x}Sr_xMnO₃ samples can be deconvoluted following the same procedure as that followed for LaCoO₃.

Table 6 presents Sr/Mn and La/Mn atomic surface ratios along with ratios of lattice oxygen and segregated strontium with respect to total oxygen and strontium content, respectively. Surface enrichment of Sr and La can also be observed for La_{1-x}Sr_xMnO₃. In contrast, segregated strontium versus total strontium content shows a constant value irrespective of strontium doping degree, which reveals a larger accommodation capacity of Sr in the lattice of La_{1-x}Sr_xMnO₃ samples with respect to La_{1-x}Sr_xCoO₃. Note also that for the same Sr doping degree segregated strontium is much higher in La_{1-x}Sr_xCoO₃ than La_{1-x}Sr_xMnO₃.

3.2.6. NO-to-NO₂ oxidation of Sr-doped perovskites

NO-to-NO₂ oxidation capacity of Co and Mn perovskites with different Sr contents are plotted in **Fig. 9**, including the evolution of

the equilibrium conversion with temperature for the chosen reaction conditions (broken lines). The oxidation capacity of a platinum model catalyst (1.5% Pt–15% BaO/Al₂O₃) is also included in both cases for comparison purpose. Strontium doped LaCoO₃ samples further improve NO conversion in comparison to non-substituted sample, especially at intermediate temperatures. Among prepared samples, La_{0.7}Sr_{0.3}CoO₃ perovskite presented the best NO-to-NO₂ performance (**Fig. 9a**), with a maximum NO conversion of 83% at 300 °C (71% achieved with LaCoO₃, and only 34% at 410 °C with Pt-based conventional catalyst). We suggest that optimum activity of La_{0.7}Sr_{0.3}CoO₃ perovskite is the result of best balance between α oxygen species (O₂-TPD) and BET surface area. It has been observed that strontium doping promotes the formation of α oxygen species but does not induce any change in the oxidation state of Co, remaining as Co³⁺ irrespective of Sr doping. Thus, it can be deduced that higher α oxygen species implies higher oxygen mobility and higher exchange capacity between lattice and feed stream oxygen, which increases the amount of active oxygen for NO oxidation [55]. Besides, among Sr doped perovskites, La_{0.7}Sr_{0.3}CoO₃ presented high exposed surface area (20.3 m² g⁻¹). In contrast, Sr doping above 30% has a negative impact on the amount of α oxygen species and surface area due to the presence of impurities derived from Sr structural saturation, and thus results in a lower oxidation capacity.

However, Sr doping slightly promotes oxidation capacity of Mn based perovskites (**Fig. 9b**). In fact, only La_{0.9}Sr_{0.1}MnO₃ formulation presented improved NO conversion with respect to the non-substituted sample. Note that Sr doping induced minor changes in α oxygen species, which reflect lower promotion of oxygen vacancies. As above discussed, charge imbalance generated by substitution of La³⁺ by Sr²⁺ could be easily compensated by Mn⁴⁺ formation, as observed by H₂-TPR. Apparently, formation of α oxygen species promotes NO oxidation in a greater extent than the presence of Mn⁴⁺ in the perovskite. In this sense, it is worth to note that the La_{0.9}Sr_{0.1}MnO₃ formulation presented higher α oxygen species than the non-substituted sample, but no further promotion was observed with increasing Sr doping [25].

Sr promotes in a higher degree the NO-to-NO₂ oxidation capacity of Co perovskites than Mn ones, which suggests that the amount of oxygen vacancies is the key factor for this enhancement. The promotion effect is maximum at intermediate temperatures and results in shifting of the conversion curve to lower temperatures with respect to Mn-based formulations. As shown, both Co and Mn perovskite formulations achieve oxidation capacity much higher than Pt-based catalyst. This trend confirms that perovskites can be considered as excellent alternative for promotion of NO oxidation reactions in automotive catalysis.

Although many reports on NO-to-NO₂ activity of perovskite-based catalysts cannot be found in the literature, we have summarized in **Table 7** reported experiments under most similar reaction conditions to those employed in this work, with the aim of comparison for use in automotive applications. Reported optimal temperature to achieve higher NO-to-NO₂ conversion resulted in similar for most studies, i.e. 300 °C for Co-based formulations and 350 °C for Mn-based formulations. In the group of Co-based perovskites, La_{0.9}Sr_{0.1}CoO₃ monolith by Kim et al. [25] stands out because of its higher conversion (86%) under GHSV = 30,000 h⁻¹, [NO] = 400 ppm and [O₂] = 8%. Experiments in this work have been achieved under most unfavorable reaction conditions, i.e. higher space velocities (GHSV = 123,500 h⁻¹), and [NO] = 650 ppm and [O₂] = 6% in the feedstream, resulting in NO conversion of 82.5% for the optimal formulation La_{0.7}Sr_{0.3}CoO₃. Our experimental conditions were almost similar to those used by Li et al. [26], concluding in the same optimal formulation and similar NO-to-NO₂ conversion. Ma et al. [55] suggested that small substitution of Co by Fe could lightly enhance NO conversion.

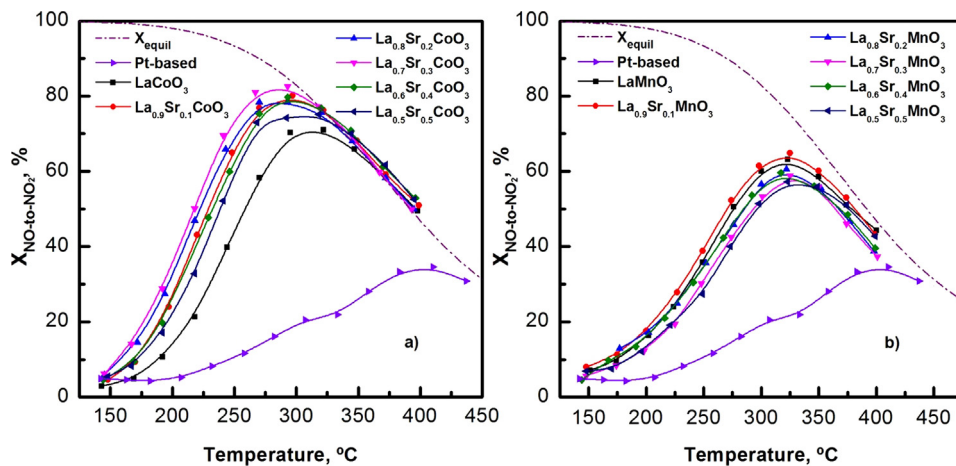


Fig. 9. NO-to-NO₂ oxidation capacity of (a) La_{1-x}Sr_xCoO₃ and (b) La_{1-x}Sr_xMnO₃ perovskites with x ranging from 0 to 0.5, together with model Pt based catalyst.

Making comparisons between Mn-based formulations, La_{0.9}MnO₃ reported by Chen et al. [14] stands out because of its high NO conversion (85%) in the presence of water and CO₂, although under most favorable reaction conditions, only 100 ppm of NO and as high as 10% O₂ in the feedstream. La_{0.9}Sr_{0.1}CoO₃ perovskite prepared in this work achieved 65% of NO-to-NO₂ conversion.

4. Conclusions

Preparation procedure of LaCoO₃ and LaMnO₃ perovskites was optimized for enhancing textural properties, and for obtaining pure perovskites, which resulted in the best NO-to-NO₂ oxidation performance. NO oxidation kinetic experiments at differential conditions ($X_{NO} < 15\%$) revealed higher intrinsic activity of LaCoO₃ than LaMnO₃ perovskite, when reaction rates were normalized per square meter of exposed surface area, and activation energies resulted in 40.5 and 17.6 kJ mol⁻¹, respectively.

Partial substitution of La by Sr in La_{1-x}Sr_xCoO₃ and La_{1-x}Sr_xMnO₃ samples affect textural properties, oxidation state of transition metal ions and formation of oxygen vacancies. Surface area was optimized for La_{0.8}Sr_{0.2}CoO₃ (21.4 m² g⁻¹) and La_{0.6}Sr_{0.4}MnO₃ (47.9 m² g⁻¹). Higher strontium doping led to the detection of strontium carbonate as a segregated phase by XRD, revealing a limited ability of perovskites to accommodate strontium in the lattice, especially for LaCoO₃, also supported by XPS analysis. The observed surface area penalization for high Sr doped perovskites could be linked to the presence of a segregated strontium phase that could block the access to the pores.

The positive charge defect due to the substitution of La³⁺ by Sr²⁺ in the La_{1-x}Sr_xCoO₃ perovskites lattice is balanced by the formation of oxygen vacancies with no modification of the oxidation state of cobalt, as it was revealed by H₂-TPR and O₂-TPD experiments. On the other hand, charge compensation in La_{1-x}Sr_xMnO₃ samples is accomplished preferably by the increase of Mn oxidation state rather than formation of oxygen vacancies.

Among the prepared catalysts La_{0.7}Sr_{0.3}CoO₃ and La_{0.9}Sr_{0.1}MnO₃ samples present the highest NO conversion, 83% and 65%, respectively, with a further improvement in comparison to non-substituted samples, 71% and 63%, respectively. Note that strontium doping is much more relevant in Co based perovskites rather than Mn based ones. The NO conversion enhancement observed for La_{0.7}Sr_{0.3}CoO₃ could be related with the higher amount of O_α species, which implies higher oxygen mobility and exchange capacity between lattice and gas phase oxygen, and also due to higher surface area. Remind that no modi-

fication of cobalt oxidation state was noticed. On the other hand, NO conversion enhancement observed for La_{0.9}Sr_{0.1}MnO₃ could be exclusively related to the higher amount of O_α species, which are not further promoted with higher strontium doping. Neither Mn⁴⁺ content nor surface area seems to be critical factors for increasing NO conversion. Perovskite formulations achieved much higher NO oxidation conversion when compared to a platinum based catalyst which makes them promising base catalysts for automobile applications.

Acknowledgments

The authors want to acknowledge the financial support supplied by the Spanish Ministry of Economy and Competitiveness (Project CTQ2015-67597-C2-1-R), Basque Government (Project IT657-13). One of the authors (JAO) acknowledges the PhD research grant (PRE_2014_1_396) by the Basque Government.

Appendix A. Supplementary data

Supplementary data associated with this article can be found, in the online version, at <http://dx.doi.org/10.1016/j.apcatb.2017.04.068>.

References

- [1] N. Takahashi, H. Shinjoh, T. Iijima, T. Suzuki, K. Yamazaki, K. Yokota, H. Suzuki, N. Miyoshi, S. Matsumoto, T. Tanizawa, T. Tanaka, S. Tateishi, K. Kasahara, *Catal. Today* 27 (1996) 63–69.
- [2] A. Russell, W.S. Epling, *Catal. Rev.* 53 (2011) 337–423.
- [3] A. Bueno-López, *Appl. Catal. B* 146 (2014) 1–11.
- [4] W.S. Epling, L.E. Campbell, A. Yezerski, N.W. Currier, J.E. Parks, *Catal. Rev.* 46 (2004) 163–245.
- [5] U. De-La-Torre, B. Pereda-Ayo, M. Moliner, J.R. González-Velasco, A. Corma, *Appl. Catal. B* 187 (2016) 419–427.
- [6] B. Pereda-Ayo, U. De La Torre, M.P. González-Marcos, J.R. González-Velasco, *Catal. Today* 241 (Pt. A) (2015) 133–142.
- [7] F. Frola, F. Prinetto, G. Ghiotti, L. Castoldi, I. Nova, L. Lietti, P. Forzatti, *Catal. Today* 126 (2007) 81–89.
- [8] B. Pereda-Ayo, U. De La Torre, M.J. Illán-Gómez, A. Bueno-López, J.R. González-Velasco, *Appl. Catal. B* 147 (2014) 420–428.
- [9] D.M. Fernandes, C.F. Scofield, A.A. Neto, M.J.B. Cardoso, F.M.Z. Zotin, *Chem. Eng. J.* 160 (2010) 85–92.
- [10] S. Ponce, M.A. Peña, J.L.G. Fierro, *Appl. Catal. B* 24 (2000) 193–205.
- [11] J. Chen, M. Shen, X. Wang, J. Wang, Y. Su, Z. Zhao, *Catal. Commun.* 37 (2013) 105–108.
- [12] Z. Gao, H. Wang, H. Ma, Z. Li, *J. Alloys Compd.* 646 (2015) 73–79.
- [13] H. Tanaka, M. Uenishi, M. Taniguchi, I. Tan, K. Narita, M. Kimura, K. Kaneko, Y. Nishihata, J. Mizuki, *Catal. Today* 117 (2006) 321–328.
- [14] J. Chen, M. Shen, X. Wang, G. Qi, J. Wang, W. Li, *Appl. Catal. B* 134–135 (2013) 251–257.

- [15] J.A. Alonso, M.J. Martínez-López, M.T. Casais, J.L. Macmanus-Driscoll, S.I.P.N.P. de Silva, L.F. Cohen, M.T.J. Fernandez-Díaz, Mater. Chem. 7 (1997) 2139–2144.
- [16] J.A.M. Van Roosmalen, E.H.P. Cordfunke, R.B. Helmholdt, H.W. Zandbergen, J. Solid State Chem. 110 (1994) 100–105.
- [17] R. Burch, P.J.F. Harris, C. Pipe, Appl. Catal. A 210 (2001) 63–73.
- [18] H. Tanaka, M. Misono, Curr. Opin. Solid State Mater. Sci. 5 (2001) 381–387.
- [19] J. Zhu, H. Li, L. Zhong, P. Xiao, X. Yang, X. Xu, X. Yang, Z. Zhao, J. Li, ACS Catal. 4 (2014) 2917–2940.
- [20] S. Royer, D. Duprez, F. Can, X. Courtois, C. Batiot-Dupeyrat, S. Laassiri, H. Alabdari, Chem. Rev. 114 (2014) 10292–10366.
- [21] R. Hammami, S.B. Aïssa, H. Batis, Appl. Catal. A 353 (2009) 145–153.
- [22] Y. Dong, H. Xian, J. Lv, C. Liu, L. Guo, M. Meng, Y. Tan, N. Tsubaki, X. Li, Mater. Chem. Phys. 143 (2014) 578–586.
- [23] F. Teng, W. Han, S. Liang, B. Gageau, R. Zong, Y. Zhu, J. Catal. 250 (2007) 1–11.
- [24] C. Zhang, W. Hua, C. Wang, Y. Guo, Y. Guo, G. Lu, A. Baylet, A. Giroir-Fendler, Appl. Catal. B 134–135 (2013) 310–315.
- [25] C.H. Kim, G. Qi, K. Dahlberg, W. Li, Science 327 (2010) 1624–1627.
- [26] X. Li, Y. Dong, H. Xian, W.Y. Hernandez, M. Meng, H. Zou, A. Ma, T. Zhang, Z. Jiang, N. Tsubaki, P. Vernoux, Energy Environ. Sci. 4 (2011) 3351–3354.
- [27] J. Zhang, D. Tan, Q. Meng, X. Weng, Z. Wu, Appl. Catal. B 172–173 (2015) 18–26.
- [28] Y. Li, L. Xue, L. Fan, Y. Yan, J. Alloys Compd. 478 (2009) 493–497.
- [29] F. Deganello, G. Marcì, G. Deganello, J. Eur. Ceram. Soc. 29 (2009) 439–450.
- [30] A. Mali, A. Ataei, Scr. Mater. 53 (2005) 1065–1070.
- [31] G. Qi, W. Li, Catal. Today 184 (2012) 72–77.
- [32] S.O. Choi, M. Penninger, C.H. Kim, W.F. Schneider, L.T. Thompson, ACS Catal. 3 (2013) 2719–2728.
- [33] W.Y. Hernández, M.N. Tsampas, C. Zhao, A. Boreave, F. Bosselet, P. Vernoux, Catal. Today 258 (Pt. 2) (2015) 525–534.
- [34] X. Yang, L. Luo, H. Zhong, Appl. Catal. A 272 (2004) 299–303.
- [35] J.L. Hueso, J.P. Holgado, R. Pérez-Gómez, V.M. González-Delacruz, A. Caballero, Mater. Chem. Phys. 151 (2015) 29–33.
- [36] S. Irusta, M.P. Pina, M. Menéndez, J. Santamaría, J. Catal. 179 (1998) 400–412.
- [37] J.A. Villoria, M.C. Alvarez-Galvan, S.M. Al-Zahrani, P. Palmisano, S. Specchia, V. Specchia, J.L.G. Fierro, R.M. Navarro, Appl. Catal. B 105 (2011) 276–288.
- [38] Y. Lu, Q. Dai, X. Wang, Catal. Commun. 54 (2014) 114–117.
- [39] H. Najjar, J. Lamonier, O. Mentré, J. Giraudon, H. Batis, Appl. Catal. B 106 (2011) 149–159.
- [40] J. Xu, J. Liu, Z. Zhao, C. Xu, J. Zheng, A. Duan, G. Jiang, J. Catal. 282 (2011) 1–12.
- [41] J. Deng, L. Zhang, H. Dai, H. He, C.T. Au, J. Mol. Catal. A: Chem. 299 (2009) 60–67.
- [42] Y. Teraoika, M. Yoshimatsu, N. Yamazoe, T. Seiyama, Chem. Lett. (1984) 893–896.
- [43] H. Wang, J. Liu, Z. Zhao, Y. Wei, C. Xu, Catal. Today 184 (2012) 288–300.
- [44] N. Yamazoe, S. Furukawa, Y. Teraoka, T. Seiyama, Chem. Lett. (1981) 1767–1770.
- [45] A. Eyssler, A. Winkler, O. Safonova, M. Nachtegaal, S.K. Matam, P. Hug, A. Weidenkaff, D. Ferri, Chem. Mater. 24 (2012) 1864–1875.
- [46] H. Arandiyán, H. Dai, J. Deng, Y. Liu, B. Bai, Y. Wang, X. Li, S. Xie, J. Li, J. Catal. 307 (2013) 327–339.
- [47] X. Li, C. Chen, C. Liu, H. Xian, L. Guo, J. Lv, Z. Jiang, P. Vernoux, ACS Catal. 3 (2013) 1071–1075.
- [48] M. Imamura, N. Matsubayashi, H. Shimada, J. Phys. Chem. B 104 (31) (2000) 7348–7353.
- [49] S. Maity, S.K. Ray, D. Bhattacharya, J. Phys. Chem. Solids 74 (2013) 315–321.
- [50] J.L.G. Fierro, L.G. Tejuca, Appl. Surf. Sci. 27 (1987) 453–457.
- [51] S. Kalagiune, A. Van Neste, V. Szabo, J.E. Gallot, M. Bassir, R. Muzychuk, Appl. Catal. A 209 (2001) 345–358.
- [52] M.M. Natile, E. Ugel, C. Maccato, A. Glisenti, Appl. Catal. B 72 (2007) 351–362.
- [53] V. Di Castro, G. Polzonetti, J. Electron Spectrosc. Relat. Phenom. 48 (1989) 117–123.
- [54] A.J. Nelson, J.G. Reynolds, J.W. Roos, J. Vac. Sci. Technol. A: Vac. Surf. Films 18 (2000) 1072–1076.
- [55] A. Ma, S. Wang, C. Liu, H. Xian, Q. Ding, L. Guo, M. Meng, Y. Tan, N. Tsubaki, J. Zhang, L. Zheng, X. Li, Appl. Catal. B 146 (2014) 24–34.